Rates of Dissipation of Turbulent Kinetic Energy in a High Reynolds Number Tidal Channel

JUSTINE M. MCMILLAN AND ALEX E. HAY

Department of Oceanography, Dalhousie University, Halifax, Nova Scotia, Canada

ROLF G. LUECK AND FABIAN WOLK

Rockland Scientific Inc., Victoria, British Columbia, Canada

(Manuscript received 14 August 2015, in final form 5 January 2016)

ABSTRACT

The ability to estimate the rate of dissipation (ε) of turbulent kinetic energy at middepth in a high-speed tidal channel using broadband acoustic Doppler current profilers (ADCPs) is assessed by making comparisons to direct measurements of ε obtained using shear probes mounted on a streamlined underwater buoy. The investigation was carried out in Grand Passage, Nova Scotia, Canada, where the depth-averaged flow speed reached $2\,\mathrm{m\,s^{-1}}$ and the Reynolds number was 8×10^7. The speed bin–averaged dissipation rates estimated from the ADCP data agree with the shear probe data to within a factor of 2. Both the ADCP and the shear probe measurements indicate a linear dependence of ε on the cube of the flow speed during flood and much lower dissipation rates during ebb. The ebb–flood asymmetry and the small-scale intermittency in ε are also apparent in the lognormal distributions of the shear probe data. Possible sources of bias and error in the ε estimates are investigated, and the most likely causes of the discrepancy between the ADCP and shear probe estimates are the cross-channel separation of the instruments and the high degree of spatial variability that exists in the channel.

1. Introduction

Measuring oceanic turbulence in high Reynolds number flows is a significant challenge for several reasons: strong flows generate high drag on instrument support structures; instrumentation techniques are limited by the spatial and temporal scales they can accurately resolve; and the turbulence itself is intermittent, in that bursts of intense energy occur at irregular intervals of time and in localized patches of space. In their 1962 benchmark study, Grant et al. (1962) overcame these challenges and successfully measured velocity fluctuations in Discovery Passage, where the Reynolds number was 3×10^8. Using a hot-film anemometer mounted on a towed body, they confirmed Kolmogorov's predicted $-5/3$ dependence of the energy spectral density on wavenumber in an inertial subrange spanning three wavenumber decades. From the velocity spectra, they also computed rates of dissipation, ε, of turbulence kinetic energy (TKE), which varied by more than a factor of 4, even though the overall nature of the flow appeared to remain the same. This intermittent behavior of the dissipation in a highly turbulent flow occurs at both large and small scales and manifests itself as sharp fluctuations in many fields—including, but not limited to, the dissipation rate, velocity, and velocity shear (Pope 2000). Intermittency, particularly at the small scales, has been the subject of several measurement campaigns in the atmospheric boundary layer; however, similar investigations in the ocean remain limited.

During the last decade, the emergence of in-stream tidal energy converters as a potential source of renewable electrical power has resulted in renewed interest in the measurement of turbulence in $O(10^8)$ Reynolds number flows. The primary need for improved knowledge of turbulence in these environments concerns the extreme and fatigue loads that large velocity and velocity shear fluctuations will exert on a turbine. Hence, an accurate characterization of both

Corresponding author address: Justine McMillan, Department of Oceanography, Dalhousie University, P.O. Box 15000, Halifax NS B3H 4R2, Canada.
E-mail: justine.mcmillan@dal.ca

DOI: 10.1175/JTECH-D-15-0167.1

the mean turbulence quantities and their variability is needed to reduce the risk associated with uncertainty in the flow conditions. Yet, making turbulence measurements at middepth—that is, the depth range swept by the turbine blades—in high-flow tidal passages represents a significant challenge. Acoustic Doppler current profiler (ADCP) techniques are attractive because their remote measurement capability greatly simplifies the instrument deployment strategy (e.g., bottom mounted), and they can simultaneously measure the mean flow, which allows for an assessment of the energy potential at a site. Several turbulence-specific ADCP measurement campaigns have been conducted in high-flow tidal channels around the world where the maximum flow speeds range from 2.5 to $4\,\mathrm{m\,s^{-1}}$ (Osalusi et al. 2009; Thomson et al. 2012; Sutherland et al. 2013; Hay et al. 2013). Other recent approaches to the acquisition of hub height turbulence measurements have involved the use of acoustic Doppler velocimeters mounted on a 5-m-high bottom frame (Thomson et al. 2012; McCaffrey et al. 2015) and on a taut-wire mooring line outfitted with inertial motion sensors (Thomson et al. 2014).

The measurement of turbulence using ADCPs is not limited to tidal energy developments. Following the introduction of the broadband version of the instrument, several studies were carried out in well-mixed tidal channels (Stacey et al. 1999; Lu and Lueck 1999; Lu et al. 2000; Rippeth et al. 2002), where the flow speeds were up to $1.5\,\mathrm{m\,s^{-1}}$ and Reynolds numbers were $O(10^7)$. These investigations implemented the variance method (Plueddemann 1987; Lohrmann et al. 1990) to make remote estimates of the Reynolds stress, turbulence production, and turbulent kinetic energy, despite the divergent beam geometry in standard ADCPs. This method requires the assumption that the fluctuations in the flow are statistically homogeneous, which is particularly limiting for bottom-mounted ADCPs in deep channels, where the beam spreading near the surface exceeds the horizontal scales of bathymetric variability. Biases can also be introduced by instrument tilt angles as low as 2° (Lu and Lueck 1999), and the determination of the TKE requires the assumption of an anisotropy ratio (Stacey et al. 1999) that is likely to vary within a given channel. Wiles et al. (2006) used the structure function approach to estimate the rate of dissipation of TKE from ADCP data, which does not require the assumption of statistical homogeneity among the beam velocities. Wiles et al. (2006) showed that the estimates of ε were dependent upon the orientation of the beams with respect to the mean flow, with the upstream-facing beam giving estimates of ε that were 3 times larger than the downstream-facing beam.

The measurement of turbulence parameters with conventional ADCPs is typically limited to first- and second-order statistical properties because high Doppler noise levels place a fundamental constraint on the accuracy of the instantaneous velocity estimates. The uncertainty in a single-ping measurement is dependent upon the sampling parameters—for standard four-beam broadband ADCPs sampling at 2 Hz, the RMS error in a beam velocity measurement is typically $O(0.05\,\mathrm{m\,s^{-1}})$, which corresponds to an uncertainty of $O(0.1\,\mathrm{m\,s^{-1}})$ in each estimate of the horizontal velocity. Because the noise is normally distributed, these errors can be reduced by computing ensembles of several measurements, however, averaging also smooths out the small-scale fluctuations that are associated with the turbulent motions of the flow. This reduced resolution, the low sampling rates (typically less than 2 Hz prior to 2014), and $O(1\,\mathrm{m})$ range cells limit the scales of the motion that can be captured. In particular, ADCPs cannot fully resolve the small-scale intermittency in the flow that Grant et al. (1962) commented on in their initial study.

Despite these limitations, ADCPs are often the instrument of choice for several reasons. The ability to measure the flow remotely enables the characterization of the undisturbed flow throughout the water column. In addition, they can be deployed for long intervals of time (months to years), allowing for an assessment of variability over a wide range of time scales. Given these advantages and the need for accurate assessments of turbulence in high Reynolds number flows, the accuracy and uncertainty of the turbulence quantities estimated from ADCPs needs to be assessed.

In this paper, we compare estimates of ε obtained directly using shear probes positioned at middepth to those made remotely using two ADCPs, one sampling at 1.5 Hz and the other at 8 Hz. At the observed Reynolds number of 8×10^7, the inertial subrange is resolved in the along-beam velocity spectra for over one wavenumber decade; thus, averaged velocity spectra are fit to the theoretical form to estimate the dissipation rate as was done by Hay et al. (2013). This approach—as opposed to the structure function method—is used, as it is not based on velocity differences that are sensitive to Doppler noise and along-beam inhomogeneity in boundary layer properties (i.e., mean shear). In this paper, we also use the shear probe measurements to obtain the probability distribution of the dissipation rate and find that it is lognormal, consistent with the form expected for intermittency of the small-scale turbulence. We also show that the dissipation rates from the ADCP data capture the same ebb–flood asymmetry in ε and its dependence on the flow speed as the shear probes.

The paper is organized as follows. First, we summarize the relevant background theory relating to turbulent boundary layer flows and dissipation rates in section 2. The deployment locations and instrumentation techniques are then described in section 3, and the data quality is assessed in section 4. Analysis methods and instrument-specific results are presented in section 5. Interinstrument comparisons and further discussion are presented in section 6, and final remarks are summarized in section 7.

2. Background and theory

a. Reynolds decomposition

In the absence of surface or internal gravity wave motions, the standard procedure used to analyze a turbulent flow is to represent the total velocity component in any direction u_i, as the sum of a mean $\overline{u_i}$ and a fluctuating part u_i':

$$u_i = \overline{u_i} + u_i'. \tag{1}$$

The separation of time scales is chosen such that over the averaging interval, the mean flow is statistically stationary and $\overline{u_i'} = 0$. Here, and for the rest of the document, an overbar is used to represent a temporal average and a prime denotes a fluctuation from the mean.

b. Isotropy and the inertial subrange

The production of turbulence occurs at large scales, where the formation of large eddies extracts energy from the mean flow. This energy then cascades to increasingly smaller scales, until eventually the smallest eddies are dissipated into heat by viscosity. At the largest scales, the flow is spatially inhomogeneous and is directionally dependent on the gradients in the mean flow (i.e., anisotropic); however, as the eddies interact with each other and pass their energy to the smaller scales, the directional biases are lost and the motions become locally isotropic.

Kolmogorov was the first to hypothesize that for sufficiently high Reynolds number flows, an inertial subrange exists where the assumption of local isotropy holds over a range of length scales. At these scales, the energy associated with the velocity fluctuations is dependent only on the rate of dissipation of TKE and a length scale associated with the eddy size. Therefore, the spectral densities ϕ of the along-channel velocity u and the vertical velocity w must satisfy

$$\phi_{uu} = C_u \varepsilon^{2/3} k^{-5/3} \quad \text{and} \tag{2}$$

$$\phi_{ww} = C_w \varepsilon^{2/3} k^{-5/3}, \tag{3}$$

where ε is the rate of dissipation; k is the radian wavenumber in the streamwise direction; and C_u and C_w are the Kolmogorov constants, given by 0.5 and 0.67, respectively (Sreenivasan 1995).

The assumption of local isotropy also allows the dissipation rate to be related to any component of the velocity shear (Hinze 1959) as

$$\varepsilon = \frac{15}{2}\nu \overline{\left(\frac{\partial u_i'}{\partial x_j}\right)^2} \quad \text{for} \quad i \neq j, \tag{4}$$

where ν is the kinematic viscosity. It follows that

$$\varepsilon = \frac{15}{2}\nu \int_0^\infty \psi(k)\, dk, \tag{5}$$

where $\psi(k)$ is the spectral density of the velocity shear. An empirical function governing ψ was developed by Nasmyth (1970) and formally published by Oakey (1982). An analytical fit to the function was initially obtained by Wolk et al. (2002); however, a slightly modified version that ensures that the integral of the shear spectrum preserves the variance of the signal is given by Lueck (2015) as

$$\psi(\tilde{k}) = \left(\frac{\varepsilon^3}{\nu}\right)^{1/4} \frac{8.05\tilde{k}^{1/3}}{1 + (20.6\tilde{k})^{3.715}}, \tag{6}$$

where $\tilde{k}$ is a nondimensional wavenumber given by $\tilde{k} = 2\pi\eta k$ and η is the Kolmogorov microscale defined by

$$\eta \equiv \left(\frac{\nu^3}{\varepsilon}\right)^{1/4}. \tag{7}$$

The form of the shear spectrum given by Eq. (6) spans both the inertial subrange and the (viscous) dissipation range.

c. Turbulent boundary layers

The flow in a high Reynolds number tidal channel is often described theoretically as a fully developed turbulent boundary layer that is formed due to flow over rough topography. If it is assumed that variations of time-averaged quantities in the streamwise direction are small and that the channel is relatively straight (i.e., no secondary circulation), then the velocity profile is expected to be self-similar in the constant stress layer near the bed (Yaglom 1979; Pope 2000). The mean flow speed in the boundary layer U_{BL} can then be described by the universal "law of the wall" given by

$$U_{\mathrm{BL}}(z) = \frac{u_*}{\kappa} \ln\left(\frac{z}{z_0}\right), \tag{8}$$

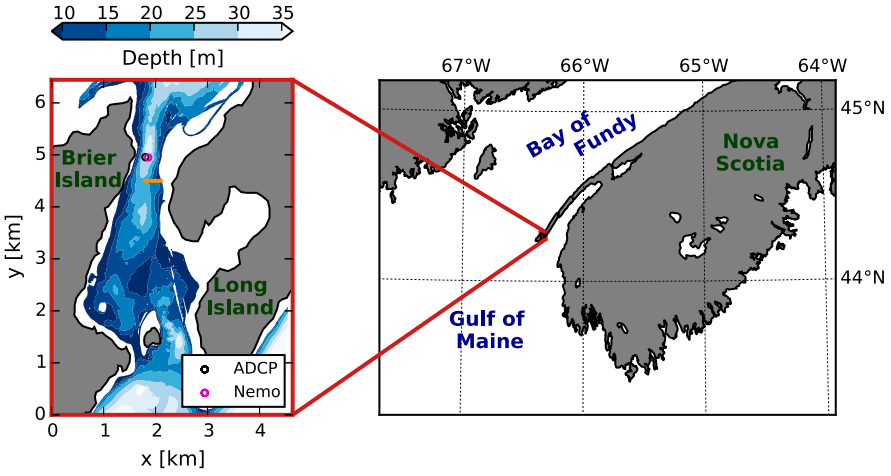

FIG. 1. Grand Passage location and bathymetry. The positions of the moored instruments are shown by the black and magenta markers, and the location of a prominent ridge is highlighted by the horizontal orange line.

where z is the height above the bottom, z_0 is the bottom roughness length scale, u_* is the friction velocity, and $\kappa = 0.4$ is the von Kármán constant. The friction velocity is defined by the bed shear stress τ_b as

$$u_* \equiv \sqrt{\frac{\tau_b}{\rho}}, \tag{9}$$

where ρ is the water density.

For wall-bounded shear flows, the production rate of TKE $\mathscr{P}$ is given by

$$\mathscr{P} = -\overline{u'w'}\frac{dU_{\mathrm{BL}}}{dz}. \tag{10}$$

Within the constant stress layer, the Reynolds stress $-\rho\overline{u'w'}$ can be equated to the bed shear stress τ_b to give

$$-\overline{u'w'} = \frac{\tau_b}{\rho}. \tag{11}$$

Equations (8)–(11) can be combined to yield an estimate for $\mathscr{P}$ in the boundary layer given by

$$\mathscr{P} = \frac{u_*^3}{\kappa z}. \tag{12}$$

Previous measurements in tidal channels have shown agreement of $\mathscr{P}$ and ε to within a factor of 2 (Rippeth et al. 2003; Osalusi et al. 2009), suggesting that in the absence of stratification, the turbulent kinetic energy is governed by a balance between the rates of production and dissipation. This suggests that the TKE has achieved a steady state and that both buoyancy and advection effects are small.

d. Taylor's hypothesis

Turbulence properties are often described in terms of spatial scales (i.e., eddy sizes); however, both the instrumentation techniques used in this study—ADCPs and shear probes—make temporal measurements of fluctuating quantities. Because turbulent eddies evolve slowly in time, the properties of the flow are assumed to be essentially "frozen" as the turbulent field is advected past a sensor by the mean flow. If the measurement interval is short compared to the time scale of the evolution of the eddies, then Taylor's frozen field hypothesis can be invoked, which allows the time ($\mathscr{T}$) and length scales ($\mathscr{L}$) to be related by

$$\mathscr{L} = \overline{U}\mathscr{T}, \tag{13}$$

where $\overline{U}$ is the mean flow speed: that is, the speed at which the turbulent field is being advected past the sensor. Taylor's hypothesis is valid provided that $k\phi_{uu}/\overline{U}^2 \ll 1$, where $u' \sim (k\phi_{uu})^{1/2}$ is an estimate of the velocity in the eddy (Huntley 1988). For the strong flows and shallow depths considered in this study, the ratio is typically much less than 0.01.

3. Dataset

a. Study site

The measurement campaign was conducted in midsummer 2013 in Grand Passage, Nova Scotia, Canada, which is located between Brier Island and Long Island (Fig. 1) at the mouth of the Bay of Fundy. The passage is about 4 km long and varies in width between 800 m and 2 km. Along the channel centerline, the water depth

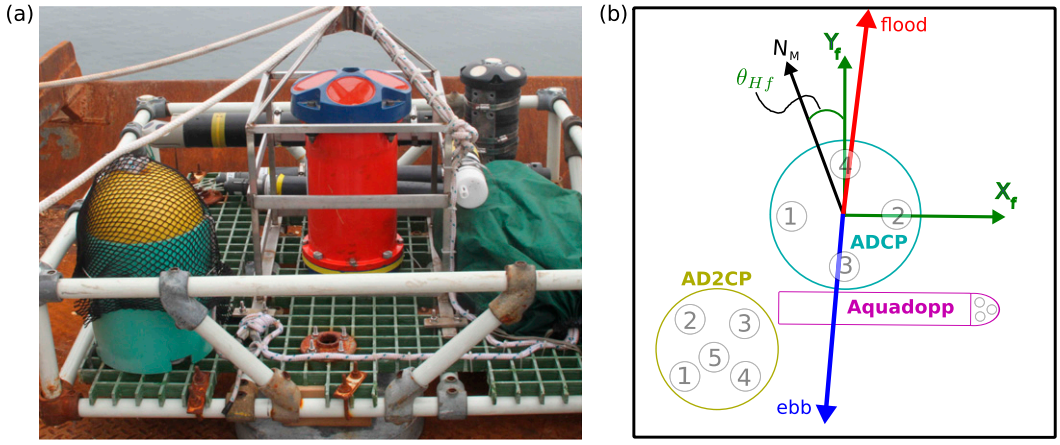

FIG. 2. (a) A picture of the bottom-mounted ADCP frame, which contains both the ADCP (orange) and the AD2CP (black). (b) The orientation of the frame with respect to magnetic north (N_M) is shown with the frame coordinates denoted by the green arrows. The circled numbers on the instruments correspond to the transducer faces for the diverging beams. The principal direction of the depth-averaged flood and ebb currents are shown by the red and blue arrows, respectively.

ranges from about 10 to 30 m and there are several bathymetric features (ridges, dune fields) that affect the flow. Peter's Island, which is located at the southern end of the passage, also generates significant eddies that are swept past the measurement site by the northward-flowing flood tide. The tidal range is about 5 m, with the M_2 constituent having the largest amplitude. The flow is highly turbulent with maximum depth-averaged speeds reaching 3 m s^{-1} (McMillan et al. 2013) and Reynolds numbers up to 8×10^7. The current flows northward on the flood tide and southward on the ebb, and is nearly rectilinear in the center of the passage. The water density varies on both seasonal and tidal time scales; however, at any given time, the water column is predominantly unstratified (Malinka 2013) due to the intense mixing generated by the eddies associated with the energetic flow. The passage is sheltered from easterly and westerly winds, and opens into fetch-limited basins to the north and south, so surface waves tend to be small, especially in midsummer. While waves did not dominate the variability in the flow at the study site, they were observed during strong ebb tides, when the southward current direction opposed the predominant northward wind. Wave occurrence is discussed further in section 5b.

b. *Bottom-mounted ADCP frame*

A bottom pod that carried three acoustic Doppler profiling instruments and an RBR Ltd. pressure sensor was deployed at the northern end of the passage (Fig. 1) where the mean water depth was 31.3 m and the channel width was approximately 1.1 km. The deployment lasted for a total of 9 days (30 July–8 August). The low-profile frame (Fig. 2a) was constructed from solid fiberglass rods and a fiberglass grating. It was ballasted using three 100-lb lead feet and recovered using an acoustic release and float line recovery system.

The primary instrument for velocity measurements was a fast-sampling 600-kHz Teledyne RD Instruments Workhorse ADCP mounted in the center of the frame (Fig. 2b). The ADCP, with beams oriented at 20° from the vertical, recorded two-ping-averaged along-beam velocities at a rate of 1.49 Hz. The ADCP was configured to have 0.5-m range bins with the first bin located 2.1 m above the bottom and the uppermost bin extending beyond the surface. To avoid acoustic interference with the other instruments, the ADCP acquired 7 min of data every 15 min.

A beta version of the Nortek 1-MHz Signature 1000 acoustic Doppler current profiler (AD2CP) was also mounted on the bottom pod and operated for almost 3.5 days before its battery died. The AD2CP has five transducers, with four beams diverging at 25° from the vertical and one beam oriented vertically. The sampling scheme was such that the four divergent beams recorded along-beam velocities at 1 Hz in forty 0.5-m range bins with the first bin located 0.6 m from the seafloor. The vertical beam was sampled at 8 Hz in forty 12.5-cm range bins to give high-resolution measurements of the vertical velocity over the lowest 5 m of the water column. The AD2CP operated in burst mode with 5 min of data collected every 15 min.

A Nortek Aquadopp was also installed on the frame; however, the velocity measurements are not used in this paper. Instead, its heading measurements were used to determine the orientation of the frame (Fig. 2b) because the compasses on both the ADCP and the AD2CP failed

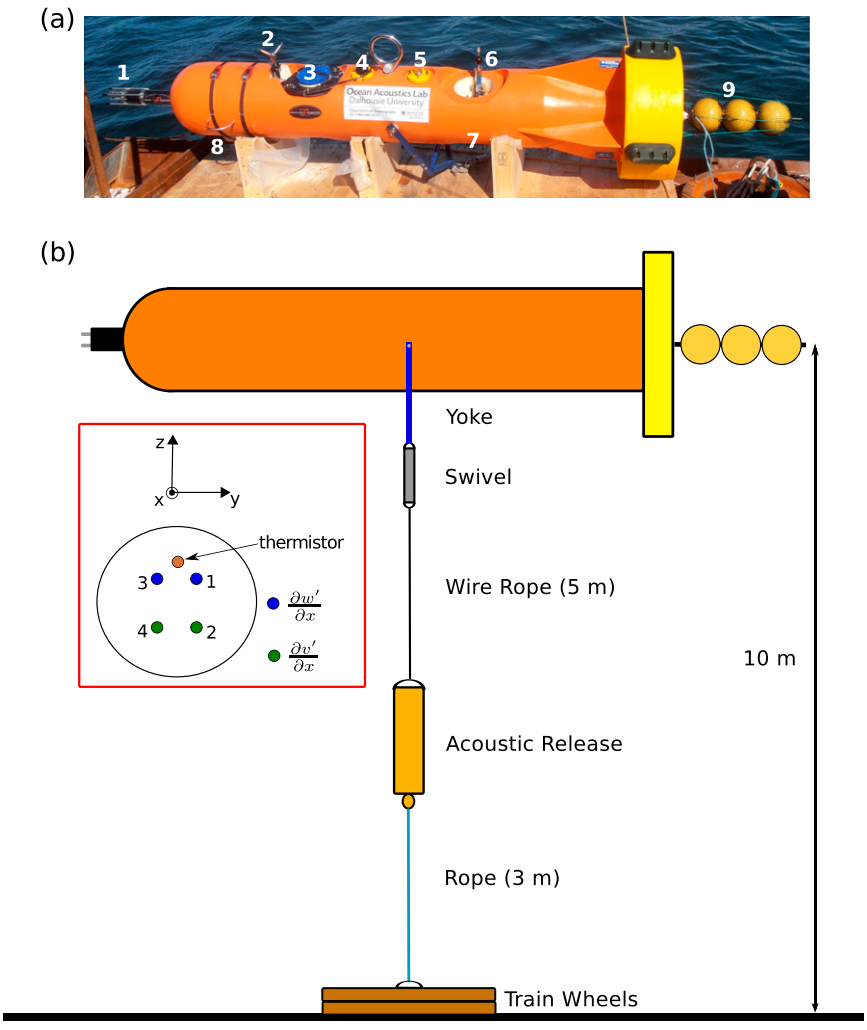

FIG. 3. (a) A photograph of the Nemo turbulence measurement system prior to deployment. The numbers correspond to the onboard instrumentation and components: 1) MicroRider, 2) ADV, 3) battery pack, 4) ADV pressure transducer, 5) satellite beacon, 6) electromagnetic current meter, 7) AD2CP, 8) extra lead weight, and 9) flotation buoys. (b) A schematic of the mooring line used to anchor Nemo. The inset shows the positions and orientations of the shear probes and the coordinate system as viewed facing the MicroRider.

to calibrate properly. At the time of deployment, the AD2CP did not have a battery calibration protocol and the ADCP would not calibrate with its installed battery.

c. *The Nemo moored turbulence system*

Between 6 and 8 August, a streamlined, instrumented underwater buoy was deployed about 40 m east of the ADCP frame (Fig. 1). The entire system, consisting of the buoy and its instrumentation, has been dubbed Nemo (Fig. 3a). The coordinate system is such that the axes are aligned with the body of the buoy: $+x$ points forward into the oncoming flow, $+y$ is to port, and $+z$ is nominally upward (Fig. 3b, inset). A similar system was used by Fer and Paskyabi (2014) in the relatively calm waters of a Norwegian fjord and by Lueck et al. (2015) in an energetic tidal channel in Scotland.

The buoy itself is about 4.5 m long and is mostly composed of syntactic foam. Nemo had a net buoyancy of 1334 N and was "flown" at a nominal height of 10 m (Fig. 3b). The buoy was free to rotate about both its horizontal and vertical axes, allowing it to pivot into the oncoming flow. Because of an error in the buoy design, it was necessary to add weight to the front of the buoy and flotation to the back. This shifted the centers of mass and buoyancy so that their net torque about the yoke axle was near zero.

Nemo carried three main instrument systems to measure both the mean and turbulent characteristics of

the flow: a Rockland Scientific Inc. (RSI) MicroRider in the nose, a Nortek acoustic Doppler velocimeter (ADV) attached to the top, and a downward-looking Nortek Signature 1000 AD2CP (beta version) just aft of the yoke axle. A battery pack that powered both the MicroRider and the ADV was mounted in the cavity just aft of the ADV. The electronics and the pressure sensor for the ADV were located immediately forward of the lifting ring. A satellite beacon and a JFE Avantech Co. electromagnetic (EM) current meter were also installed. The data from the EM current meter are in general agreement with the ADV data, but they are not used for further analysis in this paper.

The MicroRider was the primary turbulence sensor on board Nemo. This self-contained instrument carried a fast-response thermistor (temperature) probe and four airfoil shear probes, which had the ''mantle'' design described by Macoun and Lueck (2004). Two probes sensed the z component of velocity shear fluctuations and two probes that sensed the y component (Fig. 3b, inset). Two vibration sensors with their axes of sensitivity aligned with those of the probes were used to measure the inertial accelerations of the shear probes, so that vibration-related contamination could be removed from the shear probe signals. The thermistor, shear probes, and the vibration sensors were all sampled at a rate of 2048 Hz.

The MicroRider also contained several other sensors that measured the motion of Nemo at a sampling rate of 256 Hz. The mean water depth and heaving motion of the buoy were obtained using a pressure transducer. The system's pitch and roll were measured using a high-accuracy two-axis inclinometer, and the yaw was obtained using a magnetometer. A three-axis rotation rate sensor and a three-axis accelerometer were also contained within the instrument.

The ADV was used to obtain a measurement of the mean flow speed past Nemo. Results from previous experiments in Grand Passage (Hay et al. 2013) indicated that high water clarity and a lack of scatterers resulted in low correlations at high sampling rates; thus, the ADV was sampled at the minimum rate of 1 Hz. The ADV was set to use the maximum transmit power, the maximum transmit pulse length (8 mm), and the maximum sampling volume (22 mm). The ADV was mounted on the buoy such that its ''vertical'' velocity was parallel to the $+z$ axis of Nemo and the $+x$ direction was parallel to Nemo's axis of symmetry.

The downward-looking 1-MHz AD2CP was operated in bottom-tracking mode with the vertical beam sampling at 8 Hz and the diverging beams sampling at 1 Hz. The size of the range bins was 0.5 m with the center of the first bin located 0.6 m from the transducers.

4. Instrument performance and data quality

a. ADCP frame

The attitude parameters (heading, pitch, and roll) measured by the ADCP (Fig. 4a) indicate that the frame remained stable during the first week of the deployment, but it experienced a significant shift around day 218.7, when the frame rotated by about 7° and became more level (i.e., smaller pitch and roll). The data analysis presented in this paper is limited to the first 7 days of the deployment, when the frame motion was insignificant. The standard deviations of the attitude parameters within each burst were less than 0.04° for the pitch and roll, and 0.22° for the heading.

The average heading of the frame θ_{Hf} was such that beams 3 and 4 of the ADCP were oriented within 15° of the streamwise direction, whereas beams 1 and 2 pointed in the lateral direction (Fig. 2b). The pitch and roll measurements (Fig. 4a) indicate that the frame was positioned on a slight incline with beam 1 being higher than beam 2 and beam 3 being higher than beam 4. This downward slope toward the northeast is consistent with the direction of the local bathymetric gradient.

The mean correlations of the ADCP measurements in all four beams were typically within 95% of the level expected for high-quality velocity estimates (128 counts; Gordon 1996), which indicates that there was sufficient signal-to-noise ratio to generate high-fidelity ADCP data. Measurements with a correlation below 120 counts were discarded from the analysis, which resulted in the rejection of the measurements on the flood tide centered on day 212.8 (Fig. 4c, red region). The low correlations at this time were likely caused by the presence of seaweed, or some other transitory obstruction, on the transducer face. The AD2CP measurements were also of high quality with only 4% of the data being rejected due to erroneous measurements (identified by the error flag generated by Nortek's software).

b. Nemo buoy

The average flow speed past the buoy was computed in 2-min ensembles from the ADV data, discarding measurements with correlations below 70%. The maximum speed on both the flood and ebb tides reached approximately 2.2 m s^{-1} (Fig. 5a). Velocity measurements from the second range bin of the downward-looking AD2CP were only 5% less than the ADV measurements (not shown), confirming that the ADV measurement volume was positioned outside of the boundary layer of the buoy and therefore provided an accurate measurement of the upstream flow speed.

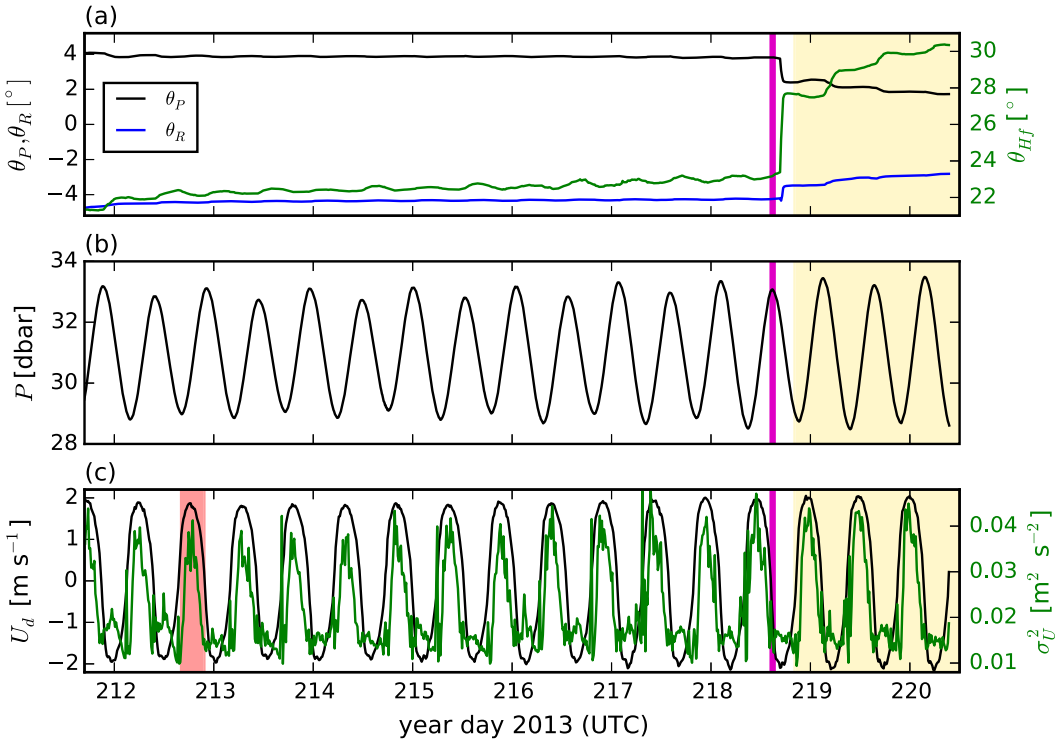

FIG. 4. Time series of the burst-averaged data from the ADCP frame. (a) ADCP attitude parameters pitch θ_P, roll θ_R, and frame heading θ_{Hf} (green). (b) Pressure as measured by the RBR Ltd. pressure sensor, (c) depth-averaged signed speed U_d, and the depth-averaged velocity variance σ_U^2 (green). The yellow shaded region corresponds to the time during which the Nemo buoy was also deployed. The red region highlights data that were rejected due to low correlations, and the majenta line indicates the end date for the analysis interval.

The bearing computed from the MicroRider magnetometer (Fig. 5a) indicates that the buoy spun around quickly at the turn of each tide (approximately 10 min for a full 180° rotation). The direction of the incoming flow as measured by the nearby ADCP (Fig. 5a, red points) agrees very well with the Nemo bearing angle.

The MicroRider roll angle remained stable throughout the deployment with an average value of 6.4 ± 0.5° (Fig. 5b). This uniform deviation from zero is an artifact caused by a misalignment in the mounting of the MicroRider, confirmed by the mean AD2CP roll of 0.3 ± 0.4°. The MicroRider pitch angle, on the other hand, was strongly correlated with flow speed, varying from about −4° during strong flows to about −35° at slack water (Fig. 5b). During flows stronger than 0.7 m s^{-1}, the magnitude of the pitch angle was typically less than 10°. The sense of rotation for the right-handed coordinate system is such that a negative pitch angle corresponds to the nose of the buoy being above the tail.

The MicroRider accelerations during strong flows were small in all three directions with mean values of 0.7, 1.1, and −0.08 m s^{-2} for A_X, A_Y, and $A_Z - 9.81$, respectively, for flow speeds greater than 1 m s^{-1} (Fig. 5c). There were some short time-scale fluctuations; however, these motions did not contaminate the shear probe signals, as they were removed from the shear spectra using a cross-correlation technique (Goodman et al. 2006).

The mean water depth above the buoy was estimated from the MicroRider pressure data, P_{MR} (Fig. 5d, black line). Near slack water, abrupt pressure drops of O(0.5 dbar) correspond to the approximately 35° pitching motion of the buoy with the nose (and hence the pressure sensor) being above the tail (Fig. 5d). During strong flows, the buoy experienced significant "blowdown" due to flow-induced drag. The associated vertical displacement of the buoy ΔD was estimated by first removing the dominant tidal signal using the pressure measurements obtained at the ADCP frame, and then calculating the mean water depth above the axle location, taking into account the pitch angle of the buoy. The resulting ΔD estimates (Fig. 5d, green line) indicate that at maximum flow, the vertical displacement was about 1 m, corresponding to a mooring line angle of about 26° from the vertical.

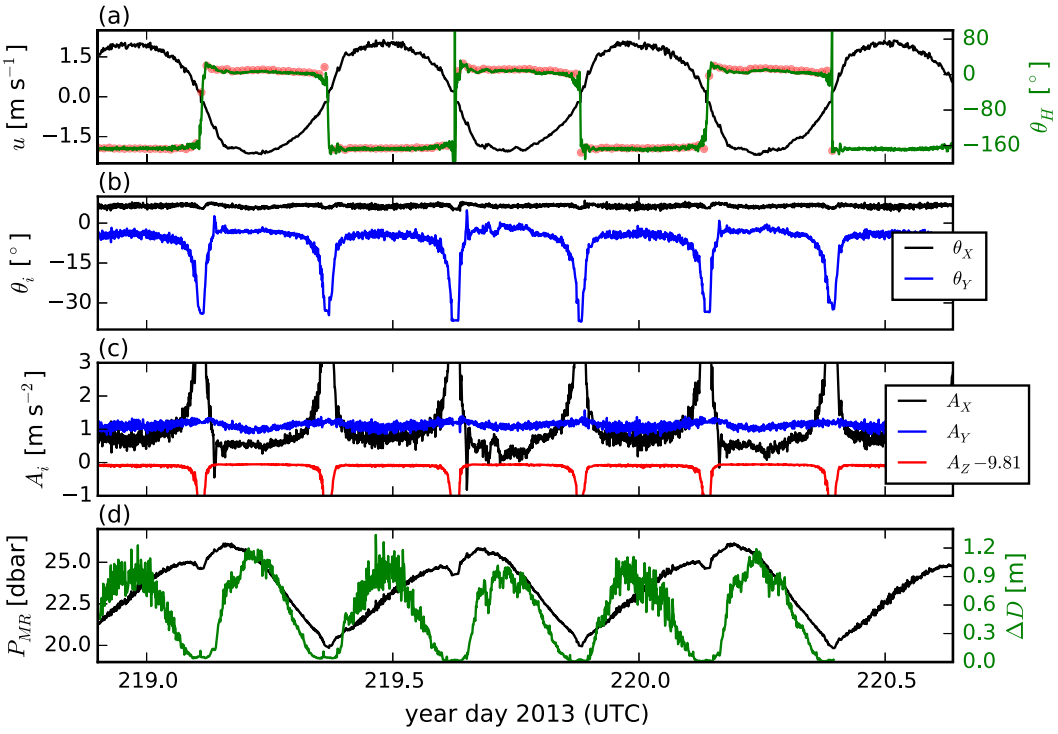

FIG. 5. Time series of the performance of Nemo throughout its deployment. (a) The signed flow speed registered by the ADV with positive representing flood (northward) flow and negative representing ebb (southward) flow. The bearing angle of the buoy as determined from the MicroRider magnetometer is plotted in green. The red markers are the direction from which the flow was coming as determined by the nearby ADCP at 10.1 m above bottom. (b) The pitch θ_Y and roll θ_X angles from the MicroRider inclinometers. (c) MicroRider accelerometer records. (d) The MicroRider pressure measurements (black) and the estimated blowdown distance of the Nemo (green).

To avoid possible contamination of the measurements by buoy tilt, data for which the absolute pitch, $|\theta_Y|$, of Nemo was greater than 10° were rejected. This resulted in the removal of 15% of the measurements; however, the buoy inclination was less than 10° for 99% of the measurements at flow speeds greater than 0.8 m s^{-1}.

5. Results

a. Mean flow

The mean and variance of the ADCP velocity measurements were computed for each 7-min burst of data (600 points). The values were then vertically averaged from the lowest range bin to 95% of the total water depth. This procedure yielded an estimate of the depth-averaged signed current speed U_d defined as

$$U_d = \pm\sqrt{u_d^2 + v_d^2}, \tag{14}$$

where the sign is used to distinguish between flood (positive) and ebb (negative) tides, and u_d and v_d are the depth-averaged components of the velocity in the east and north directions, respectively. On both the flood and the ebb tides, U_d reached 2 m s^{-1} (Fig. 4c). The depth-averaged variance σ_U^2 in U_d was about 4 times larger on the flood tide than on the ebb tide (Fig. 4c, green line) due to the presence of a ridge about 350 m south of the ADCP site. The ebb–flood asymmetry in the flow can also be observed in the speed bin–averaged velocity profiles (Fig. 6). On the flood tide, the logarithmic boundary layer extends beyond $z = 18$ m, whereas it is limited to 5–6 m above the bottom on the ebb tide. This ebb–flood asymmetry in the bottom boundary layer thickness is consistent with results presented by Hay et al. (2013) based on measurements from a bottom-mounted ADCP that was positioned just south of the ridge; that is, Hay et al. (2013) observed a much thicker logarithmic layer on the ebb tide compared to the flood tide.

b. Dissipation rates (ADCP and AD2CP)

The ADCP recorded velocity measurements along each of its four beams. Because of the beam geometry, the along-beam velocity variances σ_{Vi}^2 at a given range can be expressed as

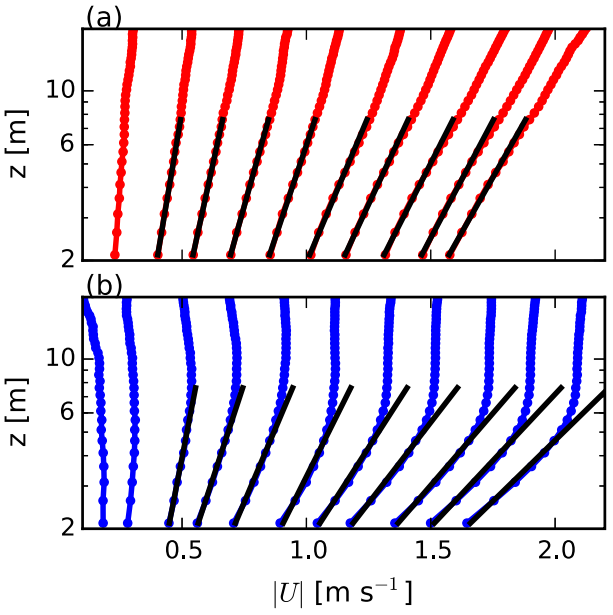

FIG. 6. Vertical profiles of the current speed as measured by the ADCP on the (a) flood tide and (b) ebb tide. The profiles, shown by the colored points. have been averaged into 0.2 m s^{-1} speed bins based on U_d. The black lines represent the nonlinear fit to the law of the wall [Eq. (8)].

$$\sigma^2_{V_1} = \sigma^2_{v_X}\sin^2\vartheta + \sigma^2_{v_Z}\cos^2\vartheta - 2\overline{v'_X v'_Z}\sin 2\vartheta + \sigma^2_{n_1}, \quad (15)$$

$$\sigma^2_{V_2} = \sigma^2_{v_X}\sin^2\vartheta + \sigma^2_{v_Z}\cos^2\vartheta + 2\overline{v'_X v'_Z}\sin 2\vartheta + \sigma^2_{n_2}, \quad (16)$$

$$\sigma^2_{V_3} = \sigma^2_{v_Y}\sin^2\vartheta + \sigma^2_{v_Z}\cos^2\vartheta - 2\overline{v'_Y v'_Z}\sin 2\vartheta + \sigma^2_{n_3}, \quad (17)$$

and

$$\sigma^2_{V_4} = \sigma^2_{v_Y}\sin^2\vartheta + \sigma^2_{v_Z}\cos^2\vartheta + 2\overline{v'_Y v'_Z}\sin 2\vartheta + \sigma^2_{n_4}, \quad (18)$$

where ϑ is the beam angle with respect to the vertical (20°); $\sigma^2_{n_i}$ is the variance introduced by Doppler noise; and v_X, v_Y, and v_Z are velocity components in frame coordinates (X_F, Y_F, Z_F), which are depicted in Fig. 2b with Z_F positive upward. Because the ADCP was oriented with beams 3 and 4 nearly aligned with the along-channel direction, Eqs. (17) and (18) can be added to yield

$$\sigma^2_{V_3} + \sigma^2_{V_4} = 2\sigma^2_u\sin^2\vartheta + 2\sigma^2_w\cos^2\vartheta + \sigma^2_{n_3} + \sigma^2_{n_4}, \quad (19)$$

where the approximations $\sigma^2_{v_Y} \approx \sigma^2_u$ and $\sigma^2_{v_Z} \approx \sigma^2_w$ are used. Following Hay et al. (2013), the velocity variances can be replaced by the spectral densities and Eqs. (2), (3), and (19) can be combined to give

$$S_T(k) = C\varepsilon^{2/3}k^{-5/3} + N_T, \quad (20)$$

where $S_T(k)$, N_T, and C are given in Table 1 (two-beam approach). Taylor's hypothesis and the conservation of variance are used to convert the spectral densities from frequency to wavenumber space. The dissipation rate can then be expressed as

$$\varepsilon = [C^{-1}(S_T - N_T)k^{5/3}]^{3/2}. \quad (21)$$

A four-beam approach was also implemented, where Eqs. (15)–(18) were summed to give

$$\sum_{b=1}^{4}\sigma_{V_b} = 2\sigma^2_u\sin^2\vartheta + 2\sigma^2_v\sin^2\vartheta + 4\sigma^2_w\cos^2\vartheta + \sum_{b=1}^{4}\sigma^2_{n_b}, \quad (22)$$

where $\sigma^2_{v_x} \approx \sigma^2_v$ represents the variance in the cross-stream direction. For the small deviation of 10°–15° between the principal flow direction and the Y_F axis, it can be assumed that $C_v = C_w$ (i.e., the cross-stream flow is orthogonal to the streamwise flow). By replacing the variances with the spectral densities, Eq. (20) can again be obtained with modified forms of $S_T(k)$, N_T, and C as given in Table 1.

The along-beam frequency spectral densities, $S_{ii}(f)$, were computed for each 7-min burst of data (600 points) within each 0.5-m vertical bin. Hanning windowed intervals of 60 points with 50% overlap were used to give 36 equivalent degrees of freedom for each estimate (Nuttall 1971) and a frequency resolution of about 0.025 Hz. The resulting spectra were then ensemble averaged over three adjacent bins in the vertical (corresponding to 1.5 m). Representative frequency spectra for beam 3 velocities are shown in Fig. 7a, where the spectra have been averaged into 0.4 m s^{-1} speed bins. The 95% confidence intervals were determined using the chi-square distribution with 36 degrees of freedom, taking into account the reduction in error by a factor of $\sqrt{n_s}$, where n_s is the total number of spectra in the speed bin ensembles. The widest and narrowest confidence intervals are plotted as vertical lines in Fig. 7a with the yellow and red colors corresponding to speed bins with the smallest and largest n_s values, respectively.

TABLE 1. Expressions for the terms in Eq. (20) for each of the methods, where $S_{ii} = S_{ii}(f)$ is the spectral density of the ith beam velocity; $\overline{U}$ is the mean speed; C_u and C_w are the streamwise and transverse Kolomogorov constants, respectively; and γ is given by Eq. (29).

Approach	$\boldsymbol{C}$	$2\pi\overline{U}^{-1}\boldsymbol{S_T(k)}$ (m^2 s^{-2} Hz^{-1})	$2\pi\overline{U}^{-1}\boldsymbol{N_T}$ (m^2 s^{-2} Hz^{-1})
Two beam	$2C_u\sin^2\vartheta + 2C_w\cos^2\vartheta$	$S_{33} + S_{44}$	$N_3 + N_4$
Two beam (tilt corrected)	$2C_u\sin^2\vartheta + 2C_w\cos^2\vartheta$	$(S_{33} + S_{44}) + \gamma(S_{33} - S_{44})$	$(N_3 + N_4) + \gamma(N_3 - N_4)$
Four beam	$2C_u\sin^2\vartheta + 2C_w\sin^2\vartheta + 4C_w\cos^2\vartheta$	$S_{11} + S_{22} + S_{33} + S_{44}$	$N_1 + N_2 + N_3 + N_4$
Vertical beam	C_w	S_{55}	N_5

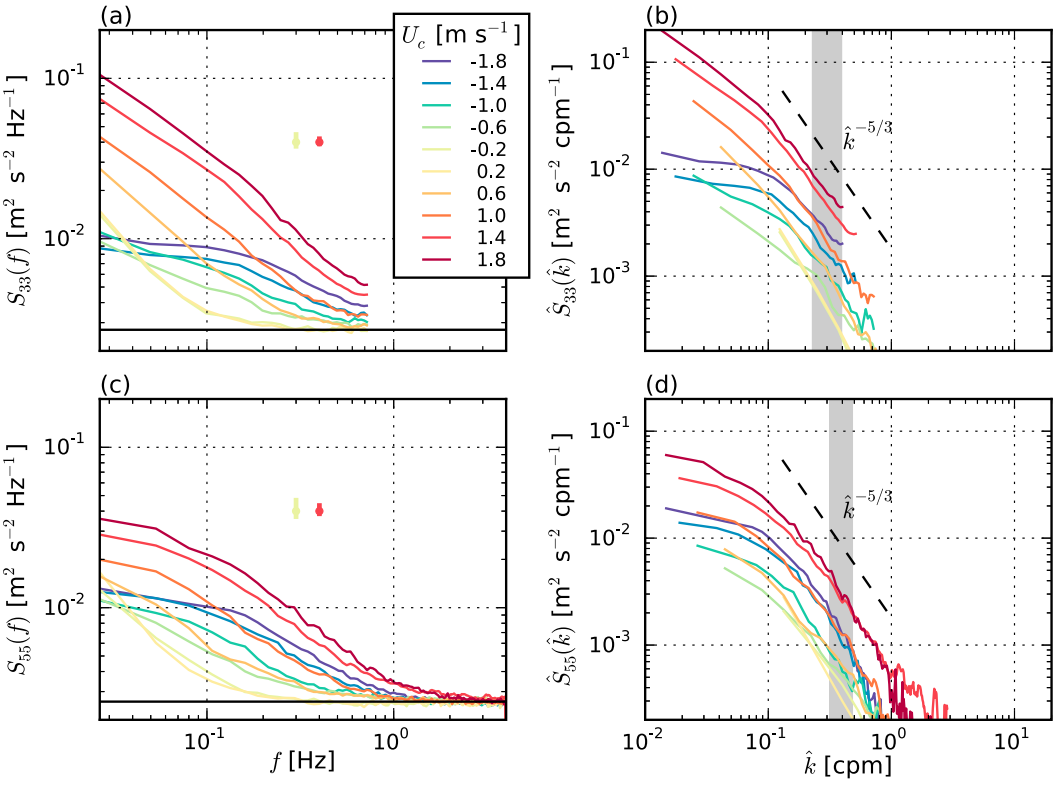

FIG. 7. Speed bin–averaged frequency and wavenumber spectra from the (a),(b) ADCP (beam 3) and (c),(d) AD2CP (beam 5) at $z = 4.6$ m. The speed bin width is 0.4 m s^{-1} with central values denoted by U_c. The vertical bars in (a) and (c) correspond to the widest (yellow) and narrowest (red) 95% confidence intervals. The gray areas in (b) and (d) correspond to the $(2\pi)^{-1}$ cpm region of the inertial subrange over which the $\varepsilon_{\rm IM}$ values were determined. The legend applies to all the subplots.

Near the 0.74-Hz Nyquist frequency (f_N), the spectra in Fig. 7a level out and approach the noise floor, N_3, represented by the black line. At this particular depth ($z = 4.6$ m), there is evidence of aliasing for the highest flow speeds ($|U_c| > 1.4$ m s^{-1}): that is, the spectral level remains above the noise floor as f approaches f_N. At distances farther from the seafloor, and hence lower turbulence levels, aliasing was not observed (not shown). For each depth and beam, the noise floor was estimated by computing the average spectral level from $f \in [0.5f_N, f_N]$ for the lowest flow speeds ($|U_c| < 0.2$ m s^{-1}). The noise floor was nearly independent of beam and depth with a mean of $(2.9 \pm 0.2) \times 10^{-3}$ m^2 s^{-2} Hz^{-1} among all estimates. Given the Nyquist frequency of 0.74 Hz, the measured noise level corresponds to a beam velocity standard deviation of 0.047 m s^{-1}, which is very close to the manufacturer-specified accuracy of 0.046 m s^{-1} based on two-ping averages and 0.5-m range bins. By subtracting the computed noise floor from the frequency spectra and implementing Taylor's hypothesis, the wavenumber spectra can be obtained. The resulting spectra for beam 3 velocities are plotted in Fig. 7b as a function of the cyclic wavenumber, $\hat{k} = (2\pi)^{-1}k$. It is apparent that the inertial subrange, where $\hat{S}_{33} \sim \hat{k}^{-5/3}$, is present for a narrow range of wavenumbers, confirming that the expected spectral shape given by Eq. (20) was observed with the ADCP data.

From the along-beam velocity spectral densities, S_T and N_T were calculated and the dissipation rate was estimated from Eq. (21) as

$$\varepsilon_{\rm IM} = [C^{-1}\langle (S_T - N_T)k^{5/3}\rangle]^{3/2}, \tag{23}$$

where the angled brackets represent the mean over the inertial subrange—that is, the integral divided by the number of points—and therefore denoted the integral method (IM). The k limits of the integration region were chosen to be the $(2\pi)^{-1}$ cycles per meter wide region that best conformed to the expected spectral shape.

Speed bin–averaged vertical profiles of $\varepsilon_{\rm IM}$ were obtained using the four-beam approach, where U_d was used to sort the data (Fig. 8a). Estimates of $\varepsilon_{\rm IM}$ with high

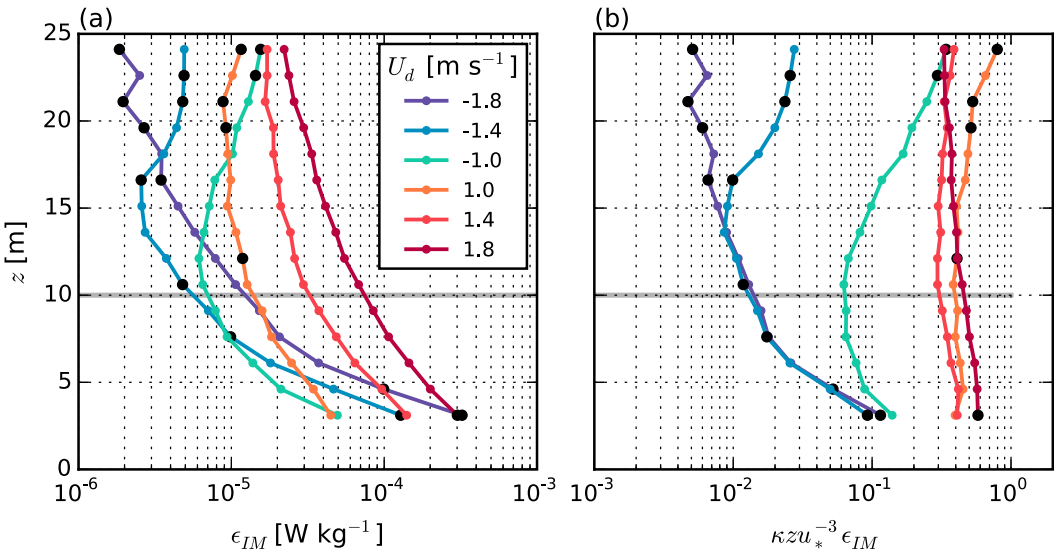

FIG. 8. Dissipation rate $\varepsilon_{\mathrm{IM}}$ as a function of height above the bottom. Profiles have been averaged into 0.4 m s^{-1} speed bins based on U_d. The thick horizontal gray lines correspond to the nominal height of Nemo. Black markers are used to indicate points with high uncertainty (see the appendix for vertical profiles of the measures of error).

uncertainty (black markers) were flagged based on at least one of the following two criteria:

1) High variability of $X = (S_T - N_T)k^{5/3}$ within the inertial subrange, that is,

$$\sigma_X > 0.1\langle X \rangle. \tag{24}$$

2) Deviation of the spectral shape of $S_T - N_T$ from the expected $-5/3$ slope in the inertial subrange, that is,

$$\frac{|\alpha|}{5/3} > 0.2, \tag{25}$$

where α is defined such that $(S_T - N_T) \sim k^{-5/3+\alpha}$.

Vertical profiles of these measures of error in the $\varepsilon_{\mathrm{IM}}$ estimates are presented in the appendix. Near the bed during strong flows, $\alpha > 0.2$, suggesting that the aliasing generated by a low sample rate and high turbulence levels causes the spectra to deviate from the $k^{-5/3}$ shape. Near the surface on the ebb tide, the measurements are contaminated by wave-induced effects. Surface wave occurrences were identified by the presence of a peak in the along-beam velocity spectra in a wave band interval of $f \in [0.1, 0.2]$ Hz. High variances over this frequency interval were observed during most strong ebb tides, despite visual observation of a calm sea state. Measurements at the Environment and Climate Change Canada meteorological station at the North Point lighthouse on Brier Island indicated that the wind speed varied between 1 and 5 m s^{-1} with a predominant northward or northeastward direction, suggesting that wind waves propagated against the southward current on the ebb, leading to wave height amplification on the ebb and not on the flood. Because the wave periods were small (~5–6-s peak period), they are deep-water waves and the increased variance associated with the wave motion does not penetrate to depths greater than 10 m.

The vertical profiles of the dissipation rate (Fig. 8a) indicate that turbulence levels are significantly higher on the flood tide compared with the ebb tide throughout the water column. For each profile, the highest dissipation rates are found near the bed, consistent with turbulence production in the bottom boundary layer. In Fig. 8b, the dissipation rates are scaled by the theoretical turbulent production given by Eq. (12) using u_* values determined from fits to the law of the wall (Fig. 6). On the flood tide, the profiles collapse to a constant value of about 0.3–0.6 for $5 < z < 15$ m, as expected for flow within the boundary layer. In contrast, the ebb tide profiles do not collapse because the log layer is much thinner and the constant stress layer was not resolved. Support for this argument was presented by Hay et al. (2013), where $u_*^2 \sim -0.4\overline{u'w'}$ at $z = 2.1$ m when the log layer was thin, suggesting that the lowest bin of the ADCP was above the constant stress layer. On the other hand, when the log layer extended beyond 15 m, Hay et al. (2013) obtained the expected result for a constant stress layer: that is, $u_*^2 \sim -\overline{u'w'}$.

Dissipation rates were also estimated from the AD2CP vertical velocities, measured directly with beam 5. Spectra for the 5-min bursts (2394 points) were

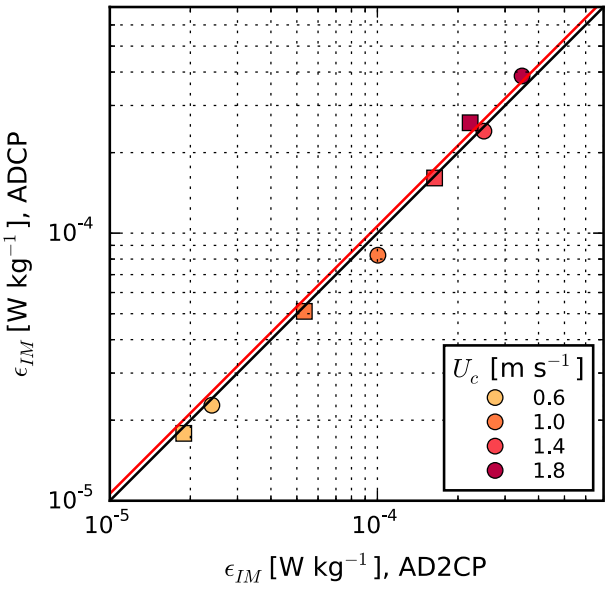

FIG. 9. Speed bin–averaged dissipation rates from the ADCP and AD2CP at heights of $z = 3.1$ m (circles) and 4.6 m (squares) on the flood tide. Colors indicate the mean speeds over the 1.5-m vertical averaging intervals. The black line is the 1:1 line, and the red line is the least squares best fit where the proportionality constant is given by 1.06.

obtained for each 12.5-cm vertical bin. Hanning windowed intervals of 300 points with 50% overlap were used, corresponding to 28 equivalent degrees of freedom (Nuttall 1971) and a frequency resolution of 0.027 Hz. The resulting spectra were then averaged over 12 adjacent range bins to obtain a 1.5-m vertical average (as for the ADCP). Representative frequency and wavenumber spectra are shown in Figs. 7c,d. Because of its higher sampling rate, the AD2CP spectra exhibit no sign of aliasing and a noise floor is apparent at $2.6 \times 10^{-3}\,\mathrm{m^2\,s^{-2}\,Hz^{-1}}$ for all speed bins. Again, the inertial subrange is clearly evident and is resolved out to $\hat{k} \sim 3$ cpm at the highest flow speeds. The dissipation rate was estimated from the AD2CP data using Eq. (23), where S_T and C are equivalent to S_{55} and C_w, respectively, because the AD2CP directly measures the vertical velocity. This approach is termed ''vertical beam'' in Table 1.

The dissipation rates estimated via IM from the ADCP (four-beam approach) and the AD2CP (vertical beam approach) at 3.1- and 4.6-m heights above bottom are compared in Fig. 9. The $\varepsilon_{\mathrm{IM}}$ values from the two instruments are linearly proportional and a least squares fit yields a proportionality constant of 1.06. This agreement indicates that errors introduced by the low sample rate and divergent beam geometry of the ADCP are small.

c. Dissipation rates (shear probes)

The 1-min mean dissipation rate was estimated from the shear probe measurements by averaging the frequency spectra computed from 119 one-second (2048 points) intervals with 50% overlap. The frequency spectra were then converted to wavenumber spectra using Taylor's hypothesis with $\overline{U}$ in Eq. (13) equated to the average flow speed $|u|$ as interpolated from the 2-min ensembles of the ADV measurements. Corrections to the spectra were made for both the spatial averaging due to the physical size of the shear probe (Macoun and Lueck 2004) and for the vibration of the instrument (Goodman et al. 2006). The 95% confidence intervals were estimated using the residual-based bootstrapping method in the frequency domain with 1000 resamples (Paparoditis 2002).

Representative shear spectra are shown in Fig. 10a for both a weakly turbulent (lower curves) and a strongly turbulent time interval (upper curves). It is clear that the spectral densities are nearly independent of probe number. The velocity spectra (Fig. 10b) are obtained by dividing the shear spectra by $(2\pi\hat{k})^2$ (Wolk et al. 2002). For the smaller wavenumbers ($\hat{k} < 30$ cpm), the spectra for both low and high turbulence intensity exhibit a well-defined inertial subrange where $\psi \sim \hat{k}^{1/3}$ and $(2\pi\hat{k})^{-2}\psi \sim \hat{k}^{-5/3}$. For the weakly turbulent case, the dissipation range—where ψ rolls off with $\hat{k}$—was captured, but was not in the highly turbulent example because the smallest eddies were not resolved by the probes. For $\hat{k} > 150$ cpm, both spectra were dominated by the attenuation effects of the antialiasing filters. The inertial subrange was much better resolved in the shear probe data than in the ADCP data, spanning nearly two decades in Fig. 10b compared to less than one decade in Fig. 7b.

As outlined by Lueck et al. (2013), ε can be computed from the shear spectra using one of two methods. For dissipation rates smaller than $2 \times 10^{-5}\,\mathrm{W\,kg^{-1}}$, the spectrum is integrated up to a maximum wavenumber $\hat{k}_{\max}$ to estimate the total variance using Eq. (5). For higher turbulence levels—since the dissipation range is not captured—the best proportional fit to the Nasmyth spectrum [Eq. (6)] is obtained over the inertial subrange, that is, $\hat{k} \in [0, \hat{k}_{\max}]$. The dissipation estimates were deemed reliable if the following criteria were satisfied:

1) The largest ratio between the ε estimates from the four probes was $10^{0.8}$, that is,

$$\frac{\max(\varepsilon_j)}{\min(\varepsilon_j)} < 10^{0.8} = 6.3, \tag{26}$$

where j is the probe number, that is, $j = 1$, 2, 3 or 4.

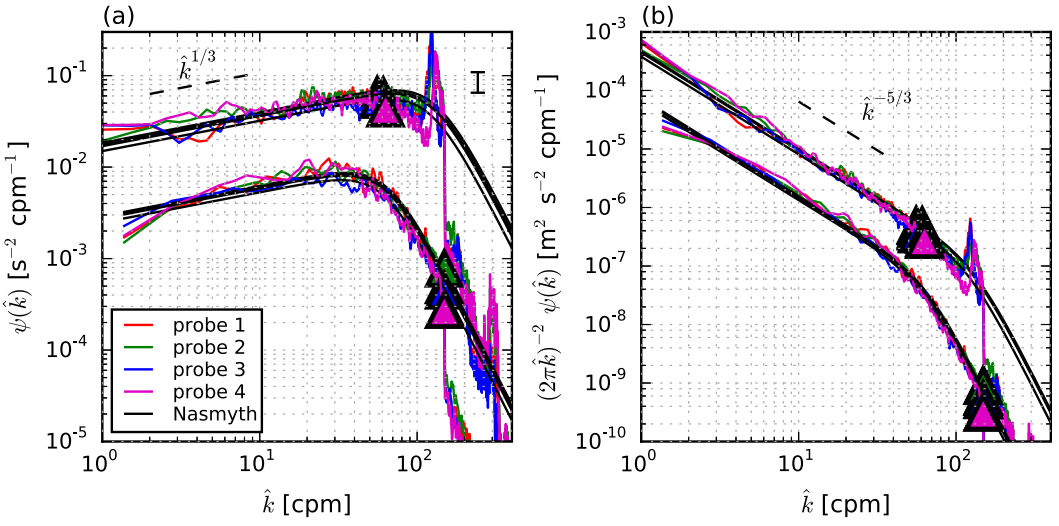

FIG. 10. One-minute-averaged (a) shear spectra and (b) velocity spectra for both a strongly turbulent region (upper curves) and a weakly turbulent region (lower curves). The triangles indicate the maximum wavenumbers $\hat{k}_{\max}$ that were used in the determination of ε for each method. The black lines represent the Nasmyth curves [Eq. (6)] for the corresponding dissipation rates ($\varepsilon \approx 1\times10^{-4}$ W kg^{-1} for the strongly turbulent region and $\varepsilon \approx 6\times10^{-6}$ W kg^{-1} for the weakly turbulent region). The error bar in the upper-right hand corner of (a) represents the mean size of the 95% confidence interval in the inertial subrange region.

2) The mean absolute deviation (MAD) of the spectra for all four probes was less than 0.4. This parameter, which was defined by Ruddick et al. (2000), is the average absolute deviation between the measured spectrum and the Nasmyth spectrum [Eq. (6)], where the average is computed over all $\hat{k}$ up to a cutoff wavenumber, $\hat{k}_{\max}$ (see section 5c). Mathematically, the MAD value is given by

$$\mathrm{MAD} = \frac{1}{n_k}\sum_{i=1}^{n_k}\left|\frac{\psi_{\mathrm{meas}}(\hat{k}_i)}{\psi_{\mathrm{Nasmyth}}(\hat{k}_i)} - 1\right|, \qquad (27)$$

where n_k is the number of discrete wavenumbers up to $\hat{k}_{\max}$.

The time series of the four-probe-average dissipation estimates is presented in Fig. 11b. The tidal variation of

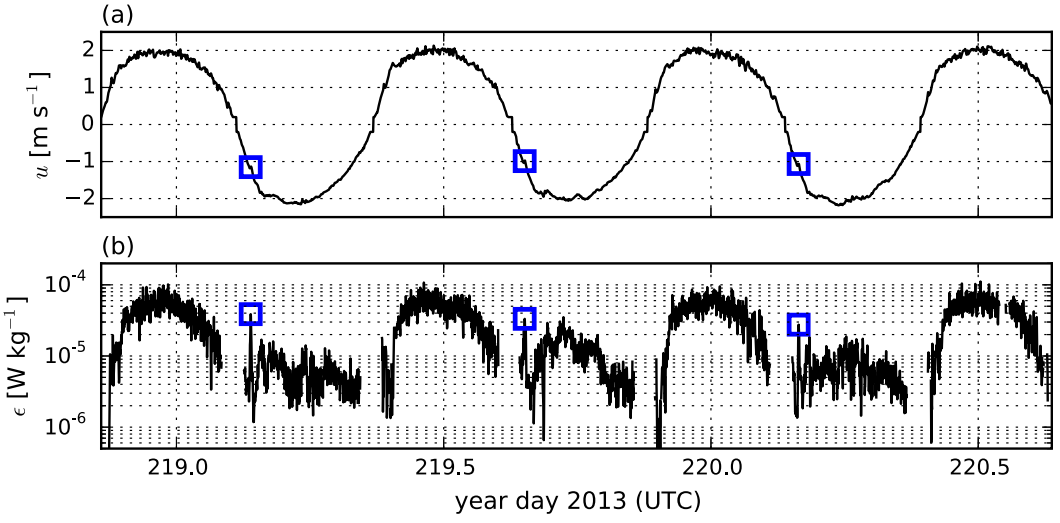

FIG. 11. (a) The signed flow speed registered by the ADV (also shown in Fig. 5a). (b) The average dissipation rate computed from the four shear probes over 1-min intervals. High dissipation rates on the ebb tide are marked by the blue squares.

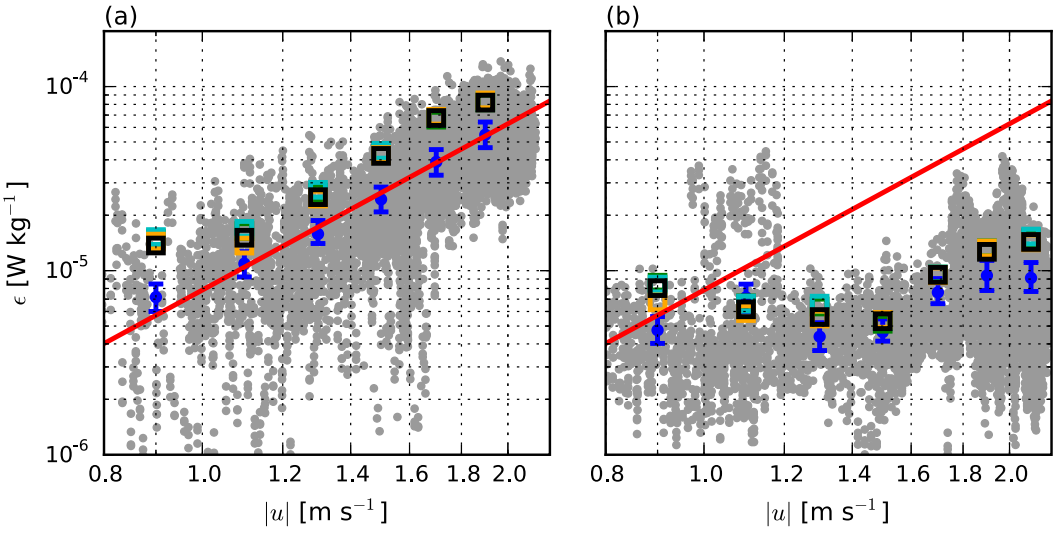

FIG. 12. Dissipation rate as a function of flow speed on the (a) flood and (b) ebb tides. The gray points represent the 1-min averages from all four shear probes. The blue markers are the mean values within speed bins 0.2 m s^{-1} in width, and the error bars represent the range of mean estimates from the four probes. The red line is $\varepsilon = 7.8 \times 10^{-6}|u|^3$, which is the LS fit to the flood tide estimates. The square markers correspond to the ε values computed from the ADCP data at $z = 10.1$ m using the four-beam IM (black), two-beam IM (green), two-beam IM with tilt correction (cyan), and LS method (yellow).

ε is clearly evident, with the flood tide values being significantly higher than those on the ebb (Figs. 11 and 12), which is qualitatively consistent with the ebb-flood asymmetry of the ADCP dissipation rates. The arithmetic mean of the values within speed bins of size 0.2 m s^{-1} is plotted as the blue markers in Fig. 12. The error bars represent the range in the mean values among the probes and not the standard deviation of the raw measurements, which is clearly much larger. On the flood tide, ε is proportional to $|u|^3$ for $|u| > 1$ m s^{-1}, where u is the measured flow speed at 10 m above the bottom. This scaling is consistent for flow in the boundary layer where turbulent production and dissipation are expected to be approximately in balance. The proportionality constant was estimated to be 7.8×10^{-6} from a least squares fit to the mean values. A $|u|^3$ dependence of ε on flow speed is not apparent during the ebb tide.

6. Discussion

a. *Interinstrument comparison of speed bin–averaged dissipation rates*

The mean values of the dissipation rate at $z = 10.1$ m computed from the ADCP data using the four-beam integral method are plotted as black squares in Fig. 12. These points exhibit the same general trends as the shear probe results on both ebb and flood, but they are higher by a factor of 1.1–1.9 (except for $|u| = 1.1$ m s^{-1} on ebb). There are a number of possible explanations for this systematic difference:

1) an error in the estimate of mean velocity due to flow distortion by the Nemo and the position of the ADV
2) the tilt of the bottom-mounted ADCP relative to the flow
3) aliasing of the ADCP spectra
4) the factor of 2 difference is real, and a consequence of the spatial separation of the two instrument platforms

The simplest of the above-mentioned possibilities is an error in the mean velocity estimate used in the implementation of Taylor's hypothesis. The flood tide results in Fig. 12a suggest that a 20% error in $|u|$ at the Nemo location would account for the difference in ε values. However, such a correction would lead to misalignment of the ebb results (Fig. 12b). Furthermore, the values of $|u|$ from the ADV differ from those computed from the AD2CP on Nemo by only 5% on average. Thus, this possibility can be dismissed.

In the derivation of Eq. (20), it is assumed that the streamlines are orthogonal to the vertical axis of the instrument coordinates. If instead it is assumed that the angle between the instrument coordinates and the streamlines is nonzero and represented by β, then Eq. (19) becomes

$$(\sigma_{V3}^2+\sigma_{V4}^2)+\gamma(\sigma_{V3}^2-\sigma_{V4}^2)=\sigma_u^2[2(\sin^2\vartheta\cos^2\beta+\cos^2\vartheta\sin^2\beta)-\cos2\vartheta\sin2\beta\tan2\beta]+\sigma_w^2[2(\cos^2\vartheta\cos^2\beta+\sin^2\vartheta\sin^2\beta)+\cos2\vartheta\sin2\beta\tan2\beta]+(\sigma_{n_3}^2+\sigma_{n_4}^2)+\gamma(\sigma_{n_3}^2-\sigma_{n_4}^2), \quad (28)$$

where

$$\gamma=\frac{\tan2\beta}{\tan2\vartheta}. \quad (29)$$

For β small, and replacing the variances with spectral densities, Eq. (20) can be obtained with S_T and N_T given by

$$S_T=\frac{\overline{U}}{2\pi}[(S_{33}+S_{44})+\gamma(S_{33}-S_{44})], \quad (30)$$

$$N_T=\frac{\overline{U}}{2\pi}[(N_3+N_4)+\gamma(N_3-N_4)], \quad (31)$$

valid to $O(\beta^2)$. The constant, C, is unchanged (Table 1). Thus, the effect of nonzero β enters through a correction term applied to S_T and N_T. This term, because it involves the product of β and the difference in spectral densities, is expected to be small.

For the current dataset, $\beta\approx0.1$ rad, as determined from the slope of the speed bin–averaged estimates of $\overline{v_Z}$ versus $\overline{v_Y}$. The corrected $\varepsilon_{\rm IM}$ values are plotted in Fig. 12 by the cyan points and are indistinguishable from the values with $\beta=0$ (green markers).

The effect of aliasing on the dissipation rates was also considered by performing a least squares fit to the speed bin–averaged spectra, taking into account the folding about the Nyquist frequency. Equation (20) can be written in the form $S_T(k_i)=ax_i+N_T$, where x_i is a summation over M folds of the wavenumber given by

$$x_i=\left[\sum_{m=0}^{M}k_m^{-5/3}\right], \quad (32)$$

where

$$k_m=\begin{cases}mk_N+k_i & \text{if } m \text{ even}\\ (m+1)k_N-k_i & \text{if } m \text{ odd}\end{cases}, \quad (33)$$

k_N is the Nyquist wavenumber, and k_i is the wavenumber in the resolved range, that is, $k_i\in[0,\,k_N]$. With the noise level N_T known, the value of a minimizing the error in the fit is

$$a=\frac{\sum_{i=1}^{n_i}S_T(k_i)x_i-N_T\sum_{i=1}^{n_i}x_i}{\sum_{i=1}^{n_i}x_i^2}, \quad (34)$$

where n_i is the total number of points in the fitting region. The dissipation rate can then be computed by

$$\varepsilon_{\rm LS}=(aC^{-1})^{3/2}, \quad (35)$$

where the subscript LS denotes least squares. Using a fitting region of $f\in[0.3,0.72]$ Hz, the $\varepsilon_{\rm LS}$ estimates at $z=10.1$ m are in good agreement with the $\varepsilon_{\rm IM}$ values (Fig. 12, red points) with the mean percent difference for all the speed bins being less than 4%. It should also be noted that the minimum error in the fit was achieved with $M=0$, thus indicating that the variance associated with the smaller, unresolved scales does not affect the spectral shapes at this depth. Closer to the bed, where aliasing is clearly prevalent (Fig. 7a), the best fits were obtained with $M=1$ (not shown).

It is possible that the differences between the ADCP and the shear probe measurements can be attributed to the 40-m cross-channel separation of the instruments. As was presented in McMillan et al. (2015), there is significant east–west variability in the dissipation rates near the deployment locations. A transect with a vertical microstructure profiler (VMP) during strong ebb flows suggested that dissipation rates at middepth were about $5\times10^{-6}\,\mathrm{W\,kg^{-1}}$ near the ADCP site and $2\times10^{-6}\,\mathrm{W\,kg^{-1}}$ near the Nemo location, which is consistent with the factor of 2 difference observed in Fig. 12. This east–west variability on the ebb tide is also supported by visual observations that were made during the deployment period. Shear lines were visible at the surface originating at the northern point of Brier Island on the ebb flow, possibly bisecting the ADCP and Nemo locations. Similar spatial variability is expected on the flood tide.

Despite the offset between the dissipation rates, this study has shown—for the first time to our knowledge—that measurements of ε made remotely using acoustic Doppler profilers are in general agreement with direct estimates from shear probes flown at middepth. The ADCP measurements successfully captured both the variation of ε with flow speed and the ebb–flood asymmetry in the turbulence levels. Previous studies have compared ADCP and shear probe estimates of ε (Rippeth et al. 2003; Wiles et al. 2006; Lucas et al. 2014; McMillan et al. 2015); however, the shear probes in these studies were mounted on vertical profilers that can only capture the instantaneous dissipation rates at a

given depth. Vertical profiles near the deployment site can be averaged together, but care must be taken to obtain meaningful averages because of the strong temporal and spatial variability of the flow. Shear probe measurements obtained using a horizontal profiler were previously compared to ADCP measurements by Lu et al. (2000); however, the comparisons were made between estimates of $\mathscr{P}$ from the ADCP and ε from the shear probes, as opposed to a direct comparison of ε, as is presented in this paper.

b. Ebb–flood asymmetry

The speed bin–averaged rates of dissipation on the flood and ebb tides are significantly different at both the ADCP and Nemo deployment locations (Figs. 8, 11, and 12). During strong flows, ε is about a factor of 10 higher on the flood tide than on the ebb tide. There is also a well-defined linear relationship between the dissipation rate and $|u|^3$ for flow speeds greater than $1\,\mathrm{m\,s^{-1}}$ during the flood (Fig. 12a). On the ebb tide, however, the ε values are more scattered and the average is comparatively independent of flow speed (Fig. 12b).

Insight into this asymmetry can be gained from the velocity profiles obtained from the ADCP measurements (Fig. 6). On the flood tide, the boundary layer is thick and extends nearly all the way to the surface. Within the boundary layer, a balance between production and dissipation is expected, and hence $\varepsilon \sim |u|^3$ as observed. On the other hand, the boundary layer is very thin on the ebb tide, so the same assumption regarding the balance cannot be made.

The channel shape also affected the dissipation rates. On the northward-flowing flood tide, the flow passes over several bathymetric features—including a prominent ridge—before reaching the deployment locations. The complex bathymetry generates macroturbulence near the bed, which then propagates upward in the water column and results in high turbulence levels at the deployment locations. On the southward-flowing ebb tide, the flow converges due to the channel shape. The associated acceleration suppresses the turbulence and hence results in lower rates of dissipation. In addition, the bathymetry at the north entrance (upstream on ebb) to the channel is less variable than that within the passage to the south (upstream on flood) of the deployment locations.

The dissipation rates at the Nemo location on the ebb tide typically range between 2×10^{-6} and $2 \times 10^{-5}\,\mathrm{W\,kg^{-1}}$ (Figs. 11b and 12b). However, there are intermittent bursts where ε remains high for several minutes at a time. One such example occurs on all three ebb tides as the flow accelerates from 1 to $1.2\,\mathrm{m\,s^{-1}}$ (Fig. 11, blue squares). The bearing of the buoy, and hence the incoming flow direction, is about 15° from true north at this time, in contrast to the mean flow direction of 5° during the stronger flows. This suggests that the flow becomes more turbulent if it passes over the shallow region to the north-northeast of the Nemo location. Greater insight into the dependence of dissipation rate on flow direction can be seen in Fig. 13, where ε is plotted as a function of the buoy pitch and the colors of the markers correspond to the bearing direction. This figure suggests that the dissipation rate is related to the pitch of the buoy, which appears to be loosely correlated to the flow direction. As the incoming flow deviates from true north, turbulence is generated by the shallow shoal and the updrafts associated with this motion cause the nose of the buoy to rotate upward. The suggestion of higher turbulence levels on the eastern side of the passage is supported by the VMP measurements that were made during the deployment period (McMillan et al. 2015).

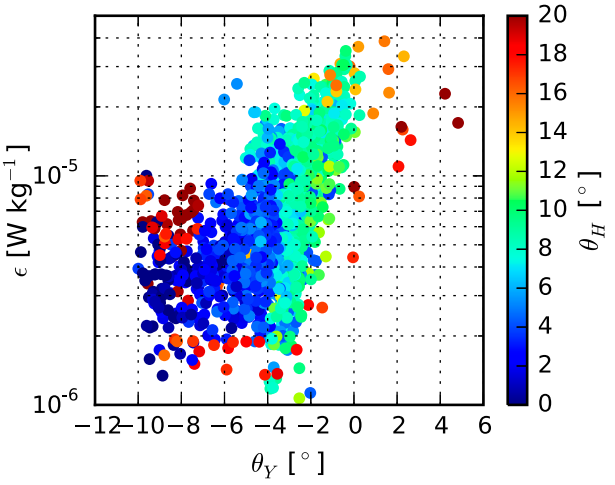

FIG. 13. Dissipation rate on the ebb tide as a function of Nemo pitch angle θ_Y (Fig. 5b). The colors of the markers correspond to the bearing of the buoy relative to true north.

c. Intermittency in the dissipation rate

The scatter in the 1-min estimates of ε (gray points in Fig. 12) is associated with small-scale intermittency, as is demonstrated by the probability density functions (PDFs) of ε (Fig. 14). These PDFs, which were computed for $|u| > 1.8\,\mathrm{m\,s^{-1}}$, are lognormal on both the flood and ebb tides. The most probable values of ε differed by 20% among the probes. The differences cannot be attributed to anisotropy because probes 1 and 3 measured fluctuations in the vertical velocity, whereas probes 2 and 4 measured fluctuations in the horizontal velocity (Fig. 3b, inset).

The flood–ebb asymmetry discussed in section 6b is again apparent in these results. The broader probability distribution on the ebb tide (Fig. 14c)—indicating a

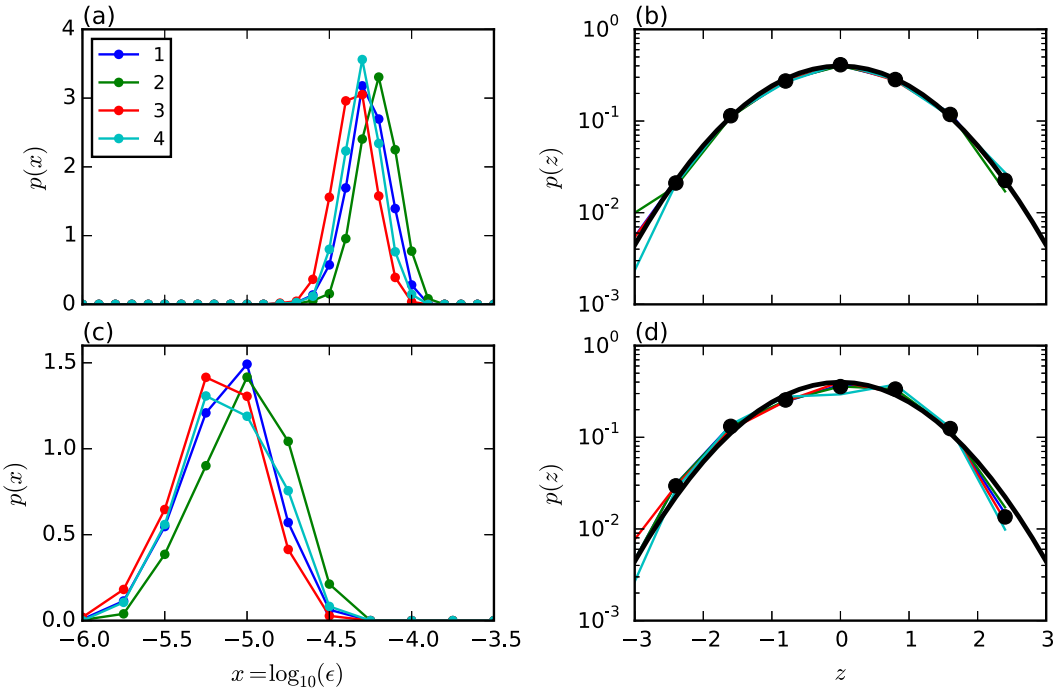

FIG. 14. PDFs of the dissipation estimates from the four shear probes for flow speeds greater than 1.8 m s^{-1}. The distributions for the (a) flood and (c) ebb tides were based on 1143 and 1021 one-minute estimates, respectively. The standardized versions of (a) and (c) are shown in (b) and (d), respectively, where $z = \sigma_x^{-1}(x - \mu_x)$, with μ_x and σ_x being the mean and standard deviation of $x = \log_{10}\varepsilon$, respectively. The black curves in the right panels are the normal distribution.

higher degree of intermittency—is likely due to the log layer being much thinner on ebb compared to flood (Fig. 6). On the ebb tide, the mean log layer is about 5 m thick; however, large-scale turbulence generates time variations in the boundary layer thickness that could cause it to periodically extend beyond 10 m. Thus, the Nemo float could have intermittently been in and out of the boundary layer on the ebb tide, generating a greater spread in the ε values. On the other hand, the presence of an 18-m-high log layer on the flood tide resulted in reduced variability in ε because the measurements were all made within the boundary layer. Because the ε values conform to the lognormal distribution (Fig. 14b), the factor of 8 spread in the 1-min estimates for $u > 1.8\,\mathrm{m\,s^{-1}}$ (Fig. 12a) is attributable to the small-scale intermittency in the boundary layer of a high Reynolds number flow.

The intermittency in the ADCP estimates of the dissipation rate was not investigated because the accuracy of the instantaneous velocity measurements is compromised by the Doppler noise. Both to properly estimate the noise level and to constrain the confidence intervals of the spectral densities, sufficient averaging of the spectra was required, allowing for an assessment of the speed bin–averaged ε values. The variability of ε at small time scales is beyond the capability of the both the IM and least squares (LS) methods presented in this paper.

7. Conclusions

Speed bin–averaged rates of dissipation of TKE at middepth in a high-flow tidal channel are estimated from bottom-mounted ADCP measurements and from shear probe measurements obtained using a horizontal profiler mounted on a streamlined underwater buoy. The two sets of ε estimates agree to within a factor of 2 but with the ADCP values consistently higher. It is shown that the discrepancy cannot be explained by 1) errors in the estimation of the mean speed of the flow past the shear probes, 2) bias induced by the tilt of the ADCP frame relative to the streamlines, or 3) aliasing in the ADCP velocity spectra due to the low sample rate. Thus, the differences are likely caused by the 40-m spatial separation of two instrument platforms. Support for this argument is provided by the cross-channel variation in ε that was observed by McMillan et al. (2013) using VMP measurements. Furthermore, comparisons between the estimates of ε from the standard, divergent beam ADCP are in better agreement (still biased high

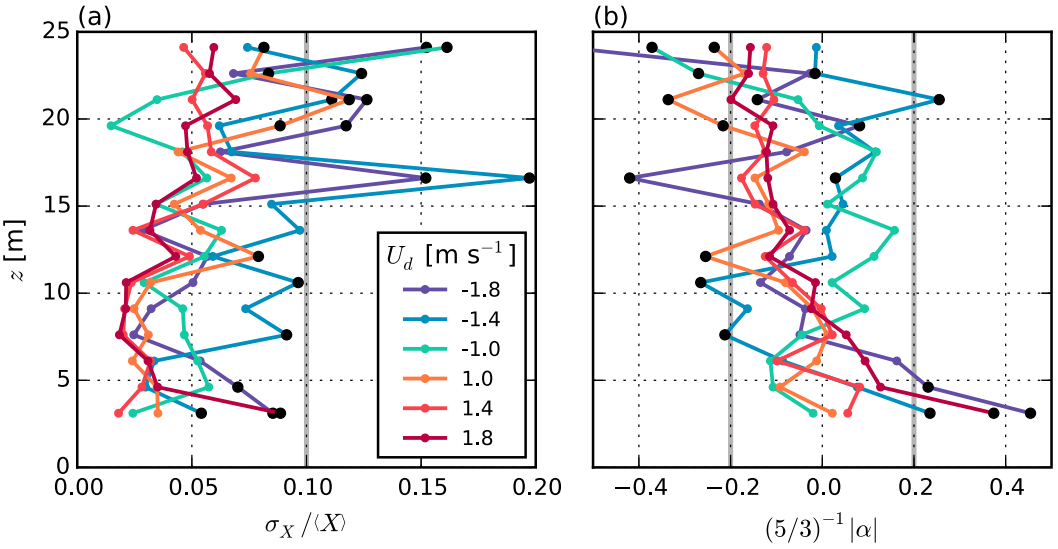

FIG. A1. Vertical profiles of the measures of error in the ε_{IM} estimates. Profiles have been averaged into 0.4 m s^{-1} speed bins based on the depth averaged speed U_d. Gray lines correspond to the thresholds used to identify uncertain estimates, and black markers denote bins where at least one of the two criteria outlined in section 5b was not satisfied.

but by only 6%) with those made by a collocated 1-MHz AD2CP (beta test version) that collected velocity measurements along its vertical beam at a sample rate of 8 Hz for $z < 5$ m.

The ADCP data captured both the variation of ε with flow speed and the ebb–flood asymmetry in the turbulence levels at middepth, consistent with the shear probe results. On the flood tide, the dissipation rate at $z = 10$ m—the nominal height of the buoy—varies with $|u|^3$ for flow speeds greater than 1 m s^{-1}, reaching a maximum value of 5×10^{-5} W kg^{-1} (as computed from the shear probe data) within the 1.9 m s^{-1} speed bin. On the ebb tide, the convergence of the flow in the narrowing channel resulted in lower dissipation rates with the maximum speed bin–averaged value of 9×10^{-6} W kg^{-1}. The dissipation rates on the ebb tide are comparatively independent of flow speed. The ebb–flood asymmetry was also apparent in probability density functions of ε computed from the shear probe measurements for $|u| > 1.8$ m s^{-1}. A broader distribution on the ebb tide suggested that the dissipation rates reflected the time variations of the boundary layer thickness generated by the large-scale turbulence.

The ADCP data were used to obtain vertical profiles of ε and hence the ebb–flood asymmetry in the flow throughout the water column. On the flood tide, an upstream ridge generates macroturbulence, causing the (logarithmic) boundary layer to extend beyond $z = 18$ m. Within this region, scaling the dissipation rates by $\mathscr{P} = (\kappa z)^{-1} u_*^3$ yields vertical profiles that are independent of height, and $\varepsilon/\mathscr{P} \sim 0.4$. In contrast, on the ebb tide the logarithmic layer is much thinner and the $\varepsilon/\mathscr{P}$ ratios were much lower and dependent on height above the bed—the maximum values were 0.1 near the bed and decayed quasi exponentially with height. Near the surface, the ebb tide estimates were contaminated with wave motion identified by the presence of a peak between 0.1 and 0.2 Hz in the velocity spectra.

The proven ability of standard, divergent beam ADCPs to make remote estimates of turbulence levels in a high Reynolds number flow is particularly promising for the tidal energy industry, which already relies heavily on these instruments for assessments of the available resource. Using the methods presented in this paper, speed bin averages of the dissipation rate can be quantified; however, the low sampling frequency and high Doppler noise levels of the ADCP limit its ability to resolve the small-scale variability in ε. On the other hand, the small physical size and fast response times of shear probes enable the high-frequency fluctuations to be resolved. The present results using the MicroRider–Nemo combination demonstrate that time series measurements of high-resolution velocity shear are attainable at middepth in high Reynolds number tidal flows. The high-sampling-rate time series, spanning several tidal cycles, gives rise to ε estimates that—for $u > 1.8$ m s^{-1}—are lognormally distributed and exhibit a factor of 8 spread within the boundary layer. Higher-order statistics are needed to fully characterize this small-scale intermittency and is the subject of ongoing work.

Acknowledgments. We thank Richard Cheel, Greg Trowse, and Peter Stern for their assistance in the field. We also acknowledge the skipper and crew of the *Saint Nicholas II* and Reid Gillis, who captained the *Island Lady G* during the completion of this work. Funding was provided by the Offshore Energy Research Association and the Natural Sciences and Engineering Research Council of Canada.

APPENDIX

Estimates of Uncertainty of ADCP ε Values

Uncertainties in the ε_{IM} estimates throughout the water column were highlighted by deviations of the speed bin–averaged velocity spectra from the expected theoretical form. Two measures of error were used to quantify the deviation as summarized in section 5b. Vertical profiles of the measures of error are shown in Fig. A1. The estimates with higher uncertainty tend to occur near the bed, near the surface, and at high flow on ebb tide.

REFERENCES

Fer, I., and M. B. Paskyabi, 2014: Autonomous ocean turbulence measurements using shear probes on a moored instrument. *J. Atmos. Oceanic Technol.*, **31**, 474–490, doi:10.1175/JTECH-D-13-00096.1.

Goodman, L., E. R. Levine, and R. G. Lueck, 2006: On measuring the terms of the turbulent kinetic energy budget from an AUV. *J. Atmos. Oceanic Technol.*, **23**, 977–990, doi:10.1175/JTECH1889.1.

Gordon, R. L., 1996: Acoustic Doppler current profiler: Principles of operation; A practical primer. RD Instruments Tech. Rep. P/N 951-6069-00, 52 pp.

Grant, H. L., R. W. Stewart, and A. Moilliet, 1962: Turbulence spectra from a tidal channel. *J. Fluid Mech.*, **12**, 241–268, doi:10.1017/S002211206200018X.

Hay, A. E., J. M. McMillan, R. Cheel, and D. J. Schillinger, 2013: Turbulence and drag in a high Reynolds number tidal passage targetted for in-stream tidal power. *Proc. Oceans 2013*, San Diego, CA, IEEE, 10 pp. [Available online at http://ieeexplore.ieee.org/xpl/login.jsp?tp=&arnumber=6741193&url=http%3A%2F%2Fieeexplore.ieee.org%2Fxpls%2Fabs_all.jsp%3Farnumber%3D6741193.]

Hinze, J. O., 1959: *Turbulence*. McGraw-Hill, 586 pp.

Huntley, D. A., 1988: A modified inertial dissipation method for estimating seabed stresses at low Reynolds numbers, with application to wave/current boundary layer measurements. *J. Phys. Oceanogr.*, **18**, 339–346, doi:10.1175/1520-0485(1988)018<0339:AMIDMF>2.0.CO;2.

Lohrmann, A., B. Hackett, and L. P. Røed, 1990: High resolution measurements of turbulence, velocity and stress using a pulse-to-pulse coherent sonar. *J. Atmos. Oceanic Technol.*, **7**, 19–37, doi:10.1175/1520-0426(1990)007<0019:HRMOTV>2.0.CO;2.

Lu, Y., and R. G. Lueck, 1999: Using a broadband ADCP in a tidal channel. Part II: Turbulence. *J. Atmos. Oceanic Technol.*, **16**, 1568–1579, doi:10.1175/1520-0426(1999)016<1568:UABAIA>2.0.CO;2.

——, ——, and D. Huang, 2000: Turbulence characteristics in a tidal channel. *J. Phys. Oceanogr.*, **30**, 855–867, doi:10.1175/1520-0485(2000)030<0855:TCIATC>2.0.CO;2.

Lucas, N. S., J. H. Simpson, T. P. Rippeth, and C. P. Old, 2014: Measuring turbulent dissipation using a tethered ADCP. *J. Atmos. Oceanic Technol.*, **31**, 1826–1837, doi:10.1175/JTECH-D-13-00198.1.

Lueck, R. G., 2015: Calculating the rate of dissipation of turbulent kinetic energy. RSI Tech. Note TN-028, 18 pp. [Available online at http://rocklandscientific.com/?wpdmdl=1034.]

——, F. Wolk, and K. Black, 2013: Measuring tidal channel turbulence with a vertical microstructure profiler (VMP). RSI Tech. Note TN-026, 35 pp. [Available online at http://rocklandscientific.com/?wpdmdl=1032.]

——, ——, J. Hancyck, and K. Black, 2015: Hub-height time series measurements of velocity and dissipation of turbulence kinetic energy in a tidal channel. *2015 IEEE/OES Eleventh Current, Waves and Turbulence Measurement Workshop (CWTM)*, IEEE, 1–5, doi:10.1109/CWTM.2015.7098143.

Macoun, P., and R. G. Lueck, 2004: Modeling the spatial response of the airfoil shear probe using different sized probes. *J. Atmos. Oceanic Technol.*, **21**, 284–297, doi:10.1175/1520-0426(2004)021<0284:MTSROT>2.0.CO;2.

Malinka, C. E., 2013: Acoustic detection ranges and baseline ambient noise measurements for a marine mammal monitoring system at a proposed in-stream tidal turbine site: Grand Passage, Nova Scotia. B.S. thesis, Dept. of Biology, Dalhousie University, 73 pp.

McCaffrey, K., B. Fox-Kemper, P. E. Hamlington, and J. Thomson, 2015: Characterization of turbulence anisotropy, coherence, and intermittency at a prospective tidal energy site: Observational data analysis. *Renewable Energy*, **76**, 441–453, doi:10.1016/j.renene.2014.11.063.

McMillan, J. M., A. E. Hay, R. H. Karsten, G. Trowse, D. Schillinger, and M. O'Flaherty-Sproul, 2013: Comprehensive tidal energy resource assessment in the lower Bay of Fundy, Canada. *Proc. 10th European Wave and Tidal Energy Conf. 2013*, Aalborg, Denmark, Aalborg University, 10 pp. [Available online at http://www.ewtec.org/proceedings/.]

——, ——, R. G. Lueck, and F. Wolk, 2015: An assessment of the turbulence at a tidal energy site using a VMP and an ADCP. *Proc. 11th European Wave and Tidal Energy Conf.*, Nantes, France, Ecole Centrale de Nantes, 8B4-4. [Available online at http://www.ewtec.org/proceedings/.]

Nasmyth, P. W., 1970: Oceanic turbulence. Ph.D. thesis, University of British Columbia, 69 pp., doi:10.14288/1.0084817.

Nuttall, A. H., 1971: Spectral estimation by means of overlapped fast Fourier transform processing of windowed data. NUSC Tech. Rep. 4169, 48 pp.

Oakey, N. S., 1982: Determination of the rate of dissipation of turbulent energy from simultaneous temperature and velocity shear microstructure measurements. *J. Phys. Oceanogr.*, **12**, 256–271, doi:10.1175/1520-0485(1982)012<0256:DOTROD>2.0.CO;2.

Osalusi, E., J. Side, and R. Harris, 2009: Reynolds stress and turbulence estimates in bottom boundary layer of Fall of Warness. *Int. Commun. Heat Mass Transfer*, **36**, 412–421, doi:10.1016/j.icheatmasstransfer.2009.02.004.

Paparoditis, E., 2002: Frequency domain bootstrap for time series. *Empirical Process Techniques for Dependent Data*, H. Dehling, T. Mikosch, and M. Sørensen, Eds., Birkhäuser, 365–381, doi:10.1007/978-1-4612-0099-4_14.

Plueddemann, A. J., 1987: Observation of the upper ocean using a multi-beam Doppler sonar. Ph.D. thesis, Scripps Institution of Oceanography, 145 pp.

Pope, S. B., 2000: *Turbulent Flows*. Cambridge University Press, 802 pp.

Rippeth, T. P., E. Williams, and J. H. Simpson, 2002: Reynolds stress and turbulent energy production in a tidal channel. *J. Phys. Oceanogr.*, **32**, 1242–1251, doi:10.1175/1520-0485(2002)032<1242:RSATEP>2.0.CO;2.

——, J. H. Simpson, E. Williams, and M. E. Inall, 2003: Measurement of the rates of production and dissipation of turbulent kinetic energy in an energetic tidal flow: Red Wharf Bay revisited. *J. Phys. Oceanogr.*, **33**, 1889–1901, doi:10.1175/1520-0485(2003)033<1889:MOTROP>2.0.CO;2.

Ruddick, B., A. Anis, and K. Thompson, 2000: Maximum likelihood spectral fitting: The Batchelor spectrum. *J. Atmos. Oceanic Technol.*, **17**, 1541–1555, doi:10.1175/1520-0426(2000)017<1541:MLSFTB>2.0.CO;2.

Sreenivasan, K. R., 1995: On the universality of the Kolmogorov constant. *Phys. Fluids*, **7**, 2778–2784, doi:10.1063/1.868656.

Stacey, M. T., S. G. Monismith, and J. R. Burau, 1999: Measurements of Reynolds stress profiles in unstratified tidal flow. *J. Geophys. Res.*, **104**, 10 933–10 949, doi:10.1029/1998JC900095.

Sutherland, D. R. J., B. G. Sellar, S. H. Harding, and I. Bryden, 2013: Initial flow characterisation utilising turbine and seabed installed acoustic sensor arrays. *Proc. 10th European Wave and Tidal Energy Conf. 2013*, Aalborg, Denmark, Aalborg University, 8 pp. [Available online at http://www.ewtec.org/proceedings/.]

Thomson, J., B. Polagye, V. Durgesh, and M. C. Richmond, 2012: Measurements of turbulence at two tidal energy sites in Puget Sound, WA. *IEEE J. Oceanic Eng.*, **37**, 363–374, doi:10.1109/JOE.2012.2191656.

——, L. F. Kilcher, and S. Harding, 2014: Multi-scale coherent turbulence at tidal energy sites. *Proc. 5th Int. Conf. on Ocean Energy*, Halifax, NS, Canada, International ICOE Committee, 6 pp. [Available online at https://www.icoe-conference.com/publication/multi-scale-coherent-turbulence-at-tidal-energy-sites/.]

Wiles, P. J., T. P. Rippeth, J. H. Simpson, and P. J. Hendricks, 2006: A novel technique for measuring the rate of turbulent dissipation in the marine environment. *Geophys. Res. Lett.*, **33**, L21608, doi:10.1029/2006GL027050.

Wolk, F., H. Yamazaki, L. Seuront, and R. G. Lueck, 2002: A new free-fall profiler for measuring biophysical microstructure. *J. Atmos. Oceanic Technol.*, **19**, 780–793, doi:10.1175/1520-0426(2002)019<0780:ANFFPF>2.0.CO;2.

Yaglom, A. M., 1979: Similarity laws for constant-pressure and pressure-gradient turbulent wall flows. *Annu. Rev. Fluid Mech.*, **11**, 505–540, doi:10.1146/annurev.fl.11.010179.002445.